Twist-controlled resonant tunnelling in graphene – boron nitride – graphene heterostructures

A. Mishchenko[1], J. S. Tu[2], Y. Cao[2], R. V. Gorbachev[2], J. R. Wallbank[3], M.T. Greenaway[4], V. E. Morozov[1], S. V. Morozov[5], M. J. Zhu[1], S. L. Wong[1], F. Withers[1], C. R. Woods[1], Y.-J. Kim[2,6], K. Watanabe[7], T. Taniguchi[7], E. E. Vdovin[4,5], O. Makarovsky[4], T. M. Fromhold[4], V. I. Fal'ko[3], A. K. Geim[1,2], L. Eaves[1,4,*], K. S. Novoselov[1,*]

[1]School of Physics & Astronomy, University of Manchester, Oxford Road, Manchester, M13 9PL, UK

[2]Centre for Mesoscience & Nanotechnology, University of Manchester, Manchester, M13 9PL, UK

[3]Physics Department, Lancaster University, LA1 4YB, UK

[4]School of Physics and Astronomy, University of Nottingham, Nottingham NG7 2RD, UK

[5]Institute of Microelectronics Technology and High Purity Materials, Russian Academy of Sciences, Chernogolovka, 142432, Russia

[6]Department of Chemistry, Seoul National University, Seoul 151-747, Korea

[7]National Institute for Materials Science, 1-1 Namiki, Tsukuba 305-0044, Japan

Recent developments in the technology of van der Waals heterostructures[1,2] made from two-dimensional atomic crystals[3,4] have already led to the observation of new physical phenomena, such as the metal-insulator transition[5] and Coulomb drag[6], and to the realisation of functional devices, such as tunnel diodes[7,8], tunnel transistors[9,10] and photovoltaic sensors[11]. An unprecedented degree of control of the electronic properties is available not only by means of the selection of materials in the stack[12] but also through the additional fine-tuning achievable by adjusting the built-in strain and relative orientation of the component layers[13-17]. Here we demonstrate how careful alignment of the crystallographic orientation of two graphene electrodes, separated by a layer of hexagonal boron nitride (hBN) in a transistor device, can achieve resonant tunnelling with conservation of electron energy, momentum and, potentially, chirality. We show how the resonance peak and negative differential conductance in the device characteristics induces a tuneable radio-frequency oscillatory current which has potential for future high frequency technology.

The growing catalogue of 2D crystals allows us to construct increasingly complex van der Waals heterostructures[7-11,18,19]. The combination of a hexagonal boron nitride barrier layer sandwiched between two graphene electrodes is particularly attractive[7,8,20] due to the exceptional crystalline quality and the small lattice mismatch of these two materials. For example, by utilising a third (gate) electrode, it has recently proved possible to make a novel type of field-effect transistor in which tunnelling between the two graphene electrodes is controlled by gate voltage[9,21]. In the prototype versions of these devices, the crystalline lattices of the component layers were not intentionally aligned[7,8,20], which meant that tunnelling between the two graphene electrodes required a defect-assisted momentum transfer, so that the tunnelling was not strictly resonant.

Here, we report on a new series of tunnel transistors in which the crystal lattices of the two graphene layers are intentionally aligned to a high degree of precision (within 2°) during the fabrication procedure. Our measurements and theoretical modelling of the device characteristics reveal that the current flow is dominated by tunnel transitions in which both energy and in-plane momentum are conserved. The resonant conditions exist in a narrow range of bias voltages, and result in a resonant peak in the current-voltage characteristics, leading to strong negative differential conductance (NDC). In the NDC region,

our devices generate radio frequency oscillations when connected to a simple *inductor-capacitor* circuit. This proof-of-principle experiment points the way towards new applications for graphene-based resonant tunnelling devices in high-frequency electronics.

A schematic diagram of our transistor is drawn on Fig. 1a, while Fig. 2a shows the dependence of the current density, J, measured at 2K as a function of the bias voltage, V_b, for three different values of the gate voltage, V_g. We observe a strong peak in $J(V_b)$, followed by a region of NDC, both of which persist up to room temperature. We attribute this peak to resonant tunnelling of carriers between the two graphene electrodes with momentum conservation. In order to display in more detail the key features of the device characteristics, Fig. 2b and c present colour scale contour maps of the dependence of the differential conductance (dI/dV_b) and d^2I/dV_b^2 on V_b and V_g; here I is current. In Fig. 2b the regions of the NDC are shown as blue areas. Furthermore, weaker resonances can be seen as a transition from pink to red colours.

In order to explain the physics of the electron tunnelling in these devices, we used a theoretical model[22-25] which takes into account the unique band structure of graphene and the physics of the eigenstates of the massless Dirac fermions in the graphene layers on the device characteristics. The results of this model, shown in Fig. 2d-f, reproduce the measured device characteristics. Here, we focus on the case of a small angular misalignment, θ, of the two graphene lattices, see Fig. 1a, which corresponds to a rotation of the two graphene Brillouin zones in *momentum* space, see Fig. 1b. In particular, the neutrality points at the six K-points of the Brillouin zone, $\hbar\boldsymbol{K}_i^{\pm}$ (where i=1,2,3 identify equivalent corners, $\pm$ distinguishes between the K and K' valleys and $\hbar$ is the reduced Plank constant) are displaced by the wavevectors $\hbar\Delta\boldsymbol{K}_i^{\pm} = \boldsymbol{l_z} \times \theta\boldsymbol{K}_i^{\pm}$.

The resulting intersection of the Dirac cones which visualise the conditions for resonant tunnelling of electrons between two layers are shown in Fig. 1c-e for characteristic regimes of bias voltage. They display the energy shift of both Dirac cones and Fermi levels as the carrier concentrations in the two graphene layers change due to changes in the bias and gate voltages. Fig. 1c and, especially, Fig. 1d illustrate how the conditions for resonant tunnelling can be satisfied. The case shown in Fig. 1d is of particular importance, since the tunnel current is maximized when the momentum difference, $\Delta\boldsymbol{K}$, is

compensated by changing electrostatically the energy of the two Dirac cones by an amount $\pm\hbar v_F \Delta K$ (valid for small θ, here v_F is the graphene Fermi velocity). In this case the conical dispersions in the two layers intersect along a straight line and a large fraction of the states along that line are occupied in one layer and empty in the other layer, thus facilitating a large resonant tunnel current. Fig. 1e demonstrates the case at yet higher bias voltage between the top and bottom graphene layers, where the in-plane momentum is conserved only for a small number of states (far away from the Fermi levels of the two graphene electrodes), thus, leading to the reduction in the current. We now consider the detailed features of the measured differential conductance map, Fig.2c. The red and blue dashed lines in Fig. 2c are theoretical simulations and correspond to the situation when Fermi levels of the top and bottom graphene layers pass through Dirac points. These lines are universal features for all graphene-to-graphene tunnelling systems regardless of their relative alignment, and can be obtained using a simple electrostatic model (see Supplementary Section 2). The density of states (*DoS*) of graphene close to the Dirac point varies linearly with chemical potential, i.e., $DoS \propto |\mu|$. Thus, the tunnel conductance decreases when the graphene Fermi level crosses the Dirac point due to the *DoS* vanishing at this point. The small but finite conductance at the Dirac point is due to charge inhomogeneity, which results in the *DoS* smearing at the Dirac point and remaining non-zero[26].

The set of green lines in Fig. 2b and c trace the low bias and relatively weak resonance in the device characteristics when the chemical potential of one of the graphene layers reaches the point where the two Dirac cones begin to overlap (Fig. 1c). These four lines satisfy the condition $\mu_{T,B} = (\Delta\varphi \pm \hbar v_F \Delta K)/2$. The intersection of these lines at $V_g = 0$ provides a good measure of the momentum mismatch $\Delta K = V_b/\hbar v_F$, and therefore gives an accurate estimate of the misalignment angle, θ. For example, for the device shown in Fig. 2, we estimate that $\theta = 1.8°$. It is interesting to note the geometry of the intersection of the two Dirac cones under the conditions shown in Fig. 1c and Fig. 2: they form hyperbolic solutions. The wavevectors of the Dirac plane waves lie on three hyperbolae obtained by 120° rotations of these hyperbolic solutions (see Supplementary Section 1). The solutions remain hyperbolic for $|\Delta\varphi| < \hbar v_F \Delta K$. This low bias resonance does not lead to NDC, but it does give rise to a significant increase in conductance, as shown in Fig. 2b.

The voltage dependence of the main resonance peak is shown as yellow lines in Fig. 2b and c. In this case, the Dirac cones are shifted by $\Delta\varphi = \pm\hbar v_F \Delta K$ so that the intersection of the cones is a straight line (i.e. the wavevectors of the Dirac plane waves lie on straight lines), see Fig. 1d. In this situation, momentum is conserved for tunnelling electrons at all energies between μ_T and μ_B, thus giving rise to a strong peak in the current density at resonance. When the Dirac cones are displaced further beyond this resonant condition, that is for $|\Delta\varphi| > \hbar v_F \Delta K$, the curve of intersection of the two Dirac cones becomes an ellipse (Fig. 1e). As a result, the wavevectors lie on three ellipses. In contrast to the hyperbolic and linear solutions, the elliptic solutions are bound – only wavevectors limited by these ellipses can contribute to current density. The reduction of the current once the Dirac cones are shifted off-resonance is the physical mechanism which gives rise to the negative differential conductance region beyond the resonant peak.

The main resonant peak, which would be Dirac-delta like in the absence of broadening, has a finite width due to the presence of short-range scatterers, charge inhomogeneity in the graphene layers or orientational disorder between two graphene layers because of bubble formation[1]. Furthermore, since this mechanism of resonant tunnelling relies on momentum conservation, the position of the resonant peak and the peak-to-valley ratio are only weakly dependent on temperature. This mechanism for NDC is only possible in the graphene-graphene tunnelling system; for example, if one or both electrodes are replaced with bilayer graphene, then, due to the parabolic dispersion relation, the extended linear intersection is no longer possible. Note that in the modelled J-V_b characteristics (Fig 2d-f) we take into account the chirality of electrons (the momentum-dependent phase shift of the wavefunction on the two sublattices in graphene, see Supplementary Sections 1 and 2). In the absence of strain, however, the results stay qualitatively the same.

In order to confirm our proposed mechanism of resonant tunnelling we performed additional measurements in which a magnetic field, $B_\parallel$, was applied parallel to the graphene layers, i.e. perpendicular to the tunnel current. Classically, the electron tunnelling between two 2D electrodes through a barrier of thickness d will acquire an additional in-plane momentum $\boldsymbol{l_z} \times \boldsymbol{B_\parallel}$, due to the action

of the Lorentz force[27,28]. Depending on the orientation of the magnetic field with respect to crystallographic directions of the two graphene layers, the magnitude of the wavevectors,

$$\hbar \Delta \boldsymbol{K}_i^{\pm} = \boldsymbol{l_z} \times \left[\theta \boldsymbol{K}_i^{\pm} + ed\boldsymbol{B}_{\parallel} \right]$$

differs for each of the six Dirac cones at the corners of Brillouin zone.

Figure 3 presents the measured (c) and calculated (d) tunnel conductance maps in the presence of a strong in-plane magnetic field, $B_{\parallel}$. In Fig. 3e, the measured contour maps at zero field (Fig. 2b) and with (Fig. 3c) magnetic field ($B_{\parallel} = 15$ T) are subtracted from each other. This "difference map" reveals that the bias positions of the resonances, which correspond to various momentum conservation conditions, are shifted significantly by the in-plane field. At the same time, the position of the $\mu_T = 0$ and $\mu_B = 0$ resonances (which are insensitive to momentum conservation) in the dI/dV_b contour maps are almost unchanged. The fact that the in-plane magnetic field affects only the resonances where momentum conservation processes are involved, rules out the possible artefacts, such as a small perpendicular component of magnetic field.

One of the celebrated applications of devices with NDC is their use as high frequency oscillators, which are typically constructed by connecting an external resonant circuit to the device. To this end, as a proof-of-principle we have built such an oscillator by adding an inductance in series with our resonant tunnelling device, while utilising the intrinsic and parasitic capacitance (C_{tot}) as a capacitance of LC circuit, see Figure 4b. When the bias and gate voltages are tuned to the NDC region, the device undergoes stable sine-wave oscillations, see Fig. 4a,c. The oscillation frequency can be tuned by varying the parameters of the external circuit, see Fig. 4b.

The operation of an NDC-based LC resonator can be understood as follows. Once excited, the LC circuit produces damped oscillations which rapidly decay to zero. This is mainly due to the internal dissipative resistance, R, of the resonator and other losses. When the tunnel transistor operates in the NDC region, its negative resistance cancels the internal lossy resistance, thus supporting continuous stable oscillations at the resonant frequency of the LC circuit. Interestingly, the shape of the J-V_b curve changes in the region of stable oscillations, as compared with the case without the LC circuit, see Figure 4a (likely, due to the

change in the asymmetric rectification of radio-frequency oscillations in the strongly nonlinear J-V_b region).

To summarize, by aligning the crystallographic orientation of the two graphene layers in a graphene-hBN-graphene heterostructure, we have demonstrated that resonant tunnelling with both energy and momentum conservation can be achieved. This results in strong NDC which persists up to room temperature. The bias position of the resonance can be controlled by the relative orientation between the two graphene crystalline lattices and by external magnetic field. Our tunnel diodes produce stable oscillations in the MHz frequency range, limited mainly by the parasitic capacitance between the contact pads of our devices and the underlying Si gate. Much higher frequencies could be reached by reducing this parasitic capacitance and that of the external circuit. Even higher frequencies could also be achieved by fabricating a device in a slot antenna configuration, where the slot acts as a resonator with resonance frequency determined by the geometry of the slot. Moreover, our tunnel devices are free of the fundamental limitation intrinsic to conventional double barrier resonant tunnelling devices, namely the relatively long carrier dwell time (~ps) in the quantum well as compared to the time to transit the barrier (~fs). This suggests that such tunnel circuits can be potentially scaled to operate in the THz regime.

Methods

Device fabrication. The heterostructures are made by means of a standard dry-transfer procedure of mechanically-exfoliated graphene and hBN layers[5,29], with the important additional step that the lattices of the top and bottom graphene flakes are aligned to within 2° of each other. We used mechanically torn graphene flakes[30] with well-defined facets and were able to distinguish between the armchair and zig-zag edges by comparing the intensity of the Raman D peak from the edges[31]. This allowed us to know the crystallographic orientation of both top and bottom graphene, thus achieving a high level of alignment (see Supplementary Section 3 for details). An independent proof of the crystallographic alignment between the two graphene electrodes comes from the measurements of the broadening of the Raman 2D peak for the two graphene flakes. Such broadening serves as a measure of the rotation angle between graphene and underlying hBN[12,32], and allows one to calculate the relative angle between the crystallographic directions for the two graphene electrodes (see Supplementary Section 3 for details). In order to improve its electronic quality, the bottom graphene electrode was placed on a thick layer of hBN overlaying the SiO$_2$/Si substrate, with the heavily doped Si wafer acting as a back gate[33]. The two graphene layers were

independently contacted with Cr/Au metallization. We chose the thickness of hBN tunnel barriers to be 4 monolayers, which allows us to work in a comfortable range of current densities and bias voltages. Note, that the current density can be dramatically increased (4-5 orders of magnitude)[7,8] if thinner (2-3 layers) hBN or a material with lower tunnel barrier (like WS_2) is utilised[9,10,18].

References

1   Geim, A. K. & Grigorieva, I. V. Van der Waals heterostructures. *Nature* **499**, 419-425 (2013).

2   Novoselov, K. S. Nobel Lecture: Graphene: Materials in the Flatland. *Reviews of Modern Physics* **83**, 837-849 (2011).

3   Novoselov, K. S. *et al.* Electric field effect in atomically thin carbon films. *Science* **306**, 666-669 (2004).

4   Novoselov, K. S. *et al.* Two-dimensional atomic crystals. *Proceedings of the National Academy of Sciences of the United States of America* **102**, 10451-10453 (2005).

5   Ponomarenko, L. A. *et al.* Tunable metal–insulator transition in double-layer graphene heterostructures. *Nature Physics* **7**, 958–961 (2011).

6   Gorbachev, R. V. *et al.* Strong Coulomb drag and broken symmetry in double-layer graphene. *Nature Physics* **8**, 896-901 (2012).

7   Lee, G. H. *et al.* Electron tunneling through atomically flat and ultrathin hexagonal boron nitride. *Applied Physics Letters* **99**, 243114 (2011).

8   Britnell, L. *et al.* Electron tunneling through ultrathin boron nitride crystalline barriers. *Nano Letters* **12**, 1707-1710 (2012).

9   Britnell, L. *et al.* Field-effect tunneling transistor based on vertical graphene heterostructures. *Science* **335**, 947-950 (2012).

10   Georgiou, T. *et al.* Vertical field-effect transistor based on graphene-WS2 heterostructures for flexible and transparent electronics. *Nature Nanotechnology* **8**, 100-103 (2013).

11   Britnell, L. *et al.* Strong light-matter interactions in heterostructures of atomically thin films. *Science* **340**, 1311-1314 (2013).

12   Woods, C. R. *et al.* Commensurate-incommensurate transition in graphene on hexagonal boron nitride. *Nature Physics* **10**, 451-456 (2014).

13   Xue, J. M. *et al.* Scanning tunnelling microscopy and spectroscopy of ultra-flat graphene on hexagonal boron nitride. *Nature Materials* **10**, 282-285 (2011).

14   Yankowitz, M. *et al.* Emergence of superlattice Dirac points in graphene on hexagonal boron nitride. *Nature Physics* **8**, 382-386 (2012).

15   Ponomarenko, L. A. *et al.* Cloning of Dirac fermions in graphene superlattices. *Nature* **497**, 594-597 (2013).

16   Dean, C. R. *et al.* Hofstadter's butterfly and the fractal quantum Hall effect in moire superlattices. *Nature* **497**, 598-602 (2013).

17   Hunt, B. *et al.* Massive Dirac fermions and Hofstadter butterfly in a van der Waals heterostructure. *Science* **340**, 1427-1430 (2013).

18   Yang, H. *et al.* Graphene barristor, a triode device with a gate-controlled Schottky barrier. *Science* **336**, 1140-1143 (2012).

19   Haigh, S. J. *et al.* Cross-sectional imaging of individual layers and buried interfaces of graphene-based heterostructures and superlattices. *Nature Materials* **11**, 764–767 (2012).

20   Britnell, L. *et al.* Resonant tunnelling and negative differential conductance in graphene transistors. *Nature Communications* **4**, 1794 (2013).

21   Ponomarenko, L. A. *et al.* Field-effect control of tunneling barrier height by exploiting graphene's low density of states. *Journal of Applied Physics* **113**, 136502 (2013).

22   Feenstra, R. M., Jena, D. & Gu, G. Single-particle tunneling in doped graphene-insulator-graphene junctions. *Journal of Applied Physics* **111**, 043711 (2012).

23   de la Barrera, S. C., Gao, Q. & Feenstra, R. M. Theory of graphene–insulator–graphene tunnel junctions. *Journal of Vacuum Science and Technology B* **32**, 04E101 (2014).

24   Wallbank, J. R. *Electronic properties of graphene heterostructures with hexagonal crystals*. (Springer, 2014).

25   Brey, L. Coherent tunneling and negative differential conductivity in a graphene/h-BN/graphene heterostructure. *Physical Review Applied* **2**, 014003 (2014).

26   Martin, J. *et al.* Observation of electron-hole puddles in graphene using a scanning single-electron transistor. *Nature Physics* **4**, 144-148 (2008).

27   Hayden, R. K. *et al.* Probing the hole dispersion curves of a quantum well using resonant magnetotunneling spectroscopy. *Physical Review Letters* **66**, 1749-1752 (1991).

28   Falko, V. I. & Meshkov, S. V. On resonant oscillations in current-voltage characteristics of double-barrier heterostructures. *Semiconductor Science and Technology* **6**, 196-200 (1991).

29   Dean, C. R. *et al.* Boron nitride substrates for high-quality graphene electronics. *Nature Nanotechnology* **5**, 722-726 (2010).

30   Sen, D., Novoselov, K. S., Reis, P. M. & Buehler, M. J. Tearing graphene sheets from adhesive substrates produces tapered nanoribbons. *Small* **6**, 1108-1116 (2010).

31   Neubeck, S. *et al.* Direct determination of the crystallographic orientation of graphene edges by atomic resolution imaging. *Applied Physics Letters* **97**, 053110 (2010).

32   Eckmann, A. *et al.* Raman fingerprint of aligned graphene/h-BN superlattices. *Nano Letters* **13**, 5242–5246 (2013).

33   Mayorov, A. S. *et al.* Micrometer-Scale Ballistic Transport in Encapsulated Graphene at Room Temperature. *Nano Letters* **11**, 2396-2399 (2011).

Acknowledgements

Author contributions

J.S.T., Y.C., and Y.J.K. fabricated devices, A.M. carried out measurements and analysed the results, J.R.W., M.T.G., T.M.F., V.I.F and L.E. provided theoretical support, K.W. and T.T. provided hBN crystals, S.L.W., F.W., and C.R.W. performed AFM and Raman measurements, R.V.G., V.E.M., S.V.M.,

M.J.Z., E.E.V., and O.M. helped with experiments and/or writing the paper, A.M., K.S.N. and L.E. wrote the manuscript. Sections 1 and 2 of Supplementary Information was written by J.R.W. and V.I.F. All authors contributed to discussions.

Additional information

Supplementary information is available in the online version of the paper. Reprints and permissions information is available online at ww.nature.com/reprints. Correspondence and requests for materials should be addressed to K.S.N. and L.E.

Competing financial interests

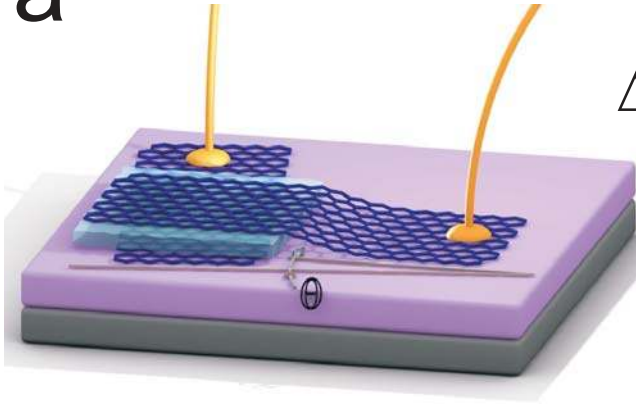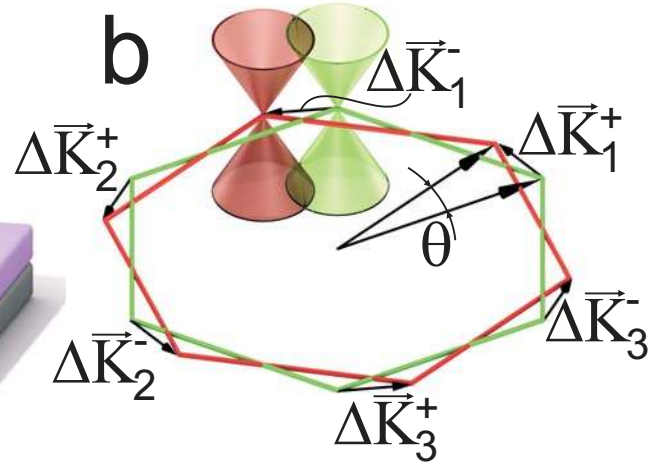The authors declare no competing financial interests.

Figure Legends

Figure 1: Schematic representation of our device and its band structure. **a)** Device schematics with the angle θ between two graphene layers (separated by a BN tunnel barrier shown in light blue) exaggerated. The heterostructure is placed on a SiO_x/Si substrate (magenta/light grey colours) serving as an electrostatic gate while both graphene layers are independently contacted by Cr/Au metallization (yellow coloured on the figure) **b)** A rotation by θ of the two graphene layers in real space corresponds to the momentum shift $\Delta K_i^{\pm}$ between two Dirac points. Diagrams **c-e** represent the relative alignment between top (left cones) and bottom (right cones) graphene Dirac points; the boundary between magenta (empty states) and blue (filled states) colours marks the Fermi level.

Figure 2. The device characteristics at 2K. Panels (a)-(c): experiment; (d)-(f): theoretical simulations. a,d) Current density-voltage curves at different V_g (red, green and blue lines for +40, 0 and -40V, respectively). b,e) Conductivity dI/dV plots as a function of V_b and V_g (colour scale is blue to white to red: -5μS to 0μS to 5μS). c,f) $|d^2I/dV^2|$ plots as a function of V_b and V_g (colour scales are arbitrary and matched for c and f). The dashed lines in b) and c) are theoretical simulations and correspond to different resonant conditions. Red and blue lines correspond to events when the Fermi level in one of the graphene layers

passes through the Dirac point. The green lines correspond to the event depicted in Fig. 1c, and the yellow line – to the event depicted in Fig. 1d. Device characteristics: active area of ≈ 8 μm^2, hBN barrier thickness is 1.4nm (4 layers), $\theta \approx 1.8°$.

Figure 3. Effect of in-plane magnetic field on resonant tunnelling, same device as in Figure 2. Panels c) and e) are experimental data, panels d) and f) – theoretical modelling. a) Trajectories of the charged quasiparticles tunnelling from top (left) to bottom (right) graphene layers in zero (black arrow) and finite (purple arrow) magnetic field (depicted as thick black arrow) due to Lorentz force. b) The resulting shift (cf. green and blue hexagons) of Fermi surface due to an in-plane magnetic field, exaggerated for clarity. Here red and green/blue hexagons represent corners of the Brillouin zones for top and bottom graphene layers, respectively. c,d) *dI/dV* maps measured with 15T in-plane magnetic field applied (colour scale is blue to white to red: -4μS to 0μS to 4μS), e,f) difference between *dI/dV* maps with and without in-plane *B* field (colour scale is blue to white to red: -0.4μS to 0μS to 0.4μS).

Figure 4. Radio-frequency oscillator based on resonant tunnelling transistor, *T*=300K. a) $J(V_b)$ characteristics with (blue, solid, *L*=1mH) and without (black, dashed, *L*=0H) external *LC* circuit. The red curve shows the V_b-dependence of the peak-to-peak amplitude of the oscillations. b) Resonant frequency of the oscillator (schematics shown on the top left inset) vs. inductance of the *LC* circuit. For this device the total capacitance of the assembly was estimated from a simple circuit model (see top left inset) to be 65pF, red line – model fit to the data. Bottom right inset: V_{out} as a function of time for *L*=1mH. c) d*I*/dV_b map measured with a 330μH inductance (red to white to blue, -0.7μS to 0μS to 0.7μS) and d) corresponding amplitude map (red to yellow to violet, 0.5V to 0.26V to 0.03V). Device structure: active area of ≈ 120 μm^2, hBN spacer =1.4nm (4 layers), $\theta \approx 0.9°$.

a

b

$\Delta\vec{K}_1^-$

$\Delta\vec{K}_2^+$

$\Delta\vec{K}_1^+$

θ

$\Delta\vec{K}_2^-$

$\Delta\vec{K}_3^-$

$\Delta\vec{K}_3^+$

c

d

e

a

b

c

d

e

f

V_b (V)

V_g (V)